

Quantum Quenches from the Critical Point: Theory and Experimental Validation in a Trapped-Ion Quantum Simulator

Chen-Xu Wang,^{1,2,3} András Grabarits^{4,*} Jin-Ming Cui,^{1,2,3,5,†} Hua-Bi Zeng,^{6,‡}

Yun-Feng Huang,^{1,2,3,5,§} Chuan-Feng Li,^{1,2,3,5,¶} and Adolfo del Campo^{4,7,**}

¹Laboratory of Quantum Information, University of Science and Technology of China, Hefei 230026, China

²Anhui Province Key Laboratory of Quantum Network,

University of Science and Technology of China, Hefei 230026, China

³CAS Center For Excellence in Quantum Information and Quantum Physics,

University of Science and Technology of China, Hefei 230026, China ^{††}

⁴Department of Physics and Materials Science, University of Luxembourg, L-1511 Luxembourg, Luxembourg

⁵Hefei National Laboratory, University of Science and Technology of China, Hefei 230088, China

⁶Center for Theoretical Physics, Hainan University, Haikou 570228, China

⁷Donostia International Physics Center, E-20018 San Sebastián, Spain

(Dated: today)

We investigate quantum quenches starting from a critical point and experimentally probe the associated defect statistics using a trapped-ion quantum simulator of the transverse-field Ising model. The cumulants of the defect number distribution exhibit universal scaling with quench depth, featuring Gaussian behavior at leading order and systematic subleading corrections. Our results are in excellent agreement with both exact and approximate theoretical predictions, establishing quench-depth scaling as a powerful and precise experimental benchmark for nonequilibrium quantum critical dynamics.

A fundamental objective in condensed matter and statistical physics is to determine the conditions under which universal behavior emerges in quantum many-body systems. In equilibrium settings, such universality, particularly near continuous phase transitions, is captured by the Ginzburg–Landau–Wilson paradigm, which classifies systems according to symmetries and spatial dimensionality via critical exponents [1].

Out of equilibrium, the emergence of universality is more subtle, but can still be captured by the Kibble–Zurek (KZ) mechanism [2–5]. This framework describes systems slowly driven across continuous phase transitions in a finite quench time τ_Q . As the control parameter g approaches its critical value g_c , the relaxation time diverges as $\tau \sim |\epsilon|^{-z\nu}$ as a function of the reduced parameter $\epsilon = (g - g_c)/g_c$, signaling a breakdown of the adiabatic dynamics near the critical point. For a linearized quench $\epsilon = t/\tau_Q$, the effective nonequilibrium relaxation time is given by the so-called freeze-out time \hat{t} , identified by the condition $\tau(\hat{t}) = \hat{t}$, resulting in $\hat{t} \sim (\tau_0 \tau_Q^{z\nu})^{1/(1+z\nu)}$. This in turn sets the nonequilibrium KZ correlation length scale $\hat{\xi} \sim |\epsilon(\hat{t})|^{-\nu}$, which determines the typical size of the domains created during the transition. As a result, the density of point-like topological defects in d spatial dimensions scales universally as $n \sim \hat{\xi}^{-d} \sim \tau_Q^{-d\nu/(1+z\nu)}$.

In the quantum regime, the KZ mechanism provides an effective framework for describing defect generation in slowly driven quantum phase transitions (QPTs) [5–8] and has become a widely used benchmark for quantum simulators and quantum computers [9–19]. Although KZ scaling accurately predicts defect formation near the adiabatic limit, in which few excitations are pro-

duced [8], it fails to capture dynamics under moderate or fast quenches. Recent studies have revealed a universal departure from the KZ behavior in this regime, where the defect density becomes governed by the final quench depth ϵ_f rather than the quench rate [20–24]. Specifically, below a characteristic quench timescale $\tau_Q \lesssim \epsilon_f^{-(z\nu+1)}$, the defect density saturates and scales as $n \sim \epsilon_f^{d\nu}$, becoming independent of τ_Q .

This breakdown of KZ scaling for the average defect number has been experimentally observed across various platforms, including confined ion chains [25–27], ion-trap quantum simulators [28], ultracold Bose and Fermi gases driven through superfluid transitions [29–32], and superconducting rings [33]. However, such studies focus on the conventional KZ setting in which a system is driven from one high-symmetry phase to a broken-symmetry phase, without addressing the universality of moderate and fast quenches.

A particularly relevant scenario arises when the quench protocol begins in the vicinity of the critical point, for example, in the frozen regime. This naturally occurs in experiments with limited tunability of control fields and restricted access to the range of system parameters. A qualitative theoretical insight based on finite-size scaling has been presented for slow quenches [34], compatible with KZ. In contrast, the fast-quench regime remains uncharted. In such a scenario, one can expect richer phenomenology and improved analytical tractability, enabling a deeper understanding of the underlying dynamics.

In this Letter, we report the experimental study of the full counting statistics of defects generated in fast quantum quenches across QPTs, using a trapped-ion quantum

simulator that realizes the one-dimensional transverse-field quantum Ising model (TFQIM). Starting from the quantum critical point, we uncover new universal scaling relations that depend on the final quench depth. We find that both the average defect pair number and its variance scale approximately linearly with the final quench depth, while the third cumulant exhibits subleading quadratic corrections. Moreover, in the slow-driving regime, we demonstrate that all cumulants follow a Kibble–Zurek-like universal scaling even when the quench commences at criticality. Finally, we show that, in both cases, defect pairs preserve their sub-Poissonian behavior, and defect numbers exhibit super-Poissonian statistics. These experimental findings are supported by exact results in the fast-quench limit and by analytical approximations combined with numerical simulations in the slow-driving regime.

TFQIM and experimental set-up. The TFQIM provides a convenient testbed of both the equilibrium properties and the non-equilibrium dynamics of QPTs [1, 7, 8, 35]. Its Hamiltonian is given by

$$\hat{\mathcal{H}}(t) = -J \sum_{m=1}^N (\hat{\sigma}_m^z \hat{\sigma}_{m+1}^z + g \hat{\sigma}_m^x), \quad (1)$$

where $\hat{\sigma}_m^{x,z}$ are the Pauli operators on the m -th spin with periodic boundary conditions, and we choose even N . Here, g controls the strength of the transverse field and $J \equiv 1$ fixes the energy scale, favoring ferromagnetic order. The second-order critical points $g_c = \pm 1$ separate the ferromagnetic ($|g| < 1$) and paramagnetic phases ($|g| > 1$). The TFQIM Hamiltonian can be mapped to the direct sum of independent two-level systems (TLSs) $\hat{\mathcal{H}}(t) = \sum_{k>0} \hat{\varphi}_k^\dagger [(g - \cos k)\sigma^z + \sin k\sigma^x] \hat{\varphi}_k = \sum_{k>0} \epsilon_k(g) \left(\hat{\gamma}_k^\dagger(t) \hat{\gamma}_k(t) + \hat{\gamma}_{-k}^\dagger(t) \hat{\gamma}_{-k}(t) - 1 \right)$, where $\hat{\varphi}_k = (\hat{c}_k, \hat{c}_{-k}^\dagger)$ contains the creation and annihilation operators and the momentum is quantized as $k = \frac{\pi}{L}, \frac{3\pi}{L}, \dots, \pi - \frac{\pi}{L}$. The momentum space Hamiltonian associated with each mode is diagonalized by the Bogoliubov operators $\hat{\gamma}_k(t)$. The corresponding eigenenergies $\epsilon_k(g)$ exhibit avoided crossings in which pairs of quasiparticle excitations in modes $(-k, k)$ are generated with Landau-Zener (LZ) transition probabilities p_k , under a slow linear ramping of the form $g(t) = g(0) + t/\tau_Q$ [7, 9]. For processes terminating at $g(\tau_Q) = 0$, the average number of pairs of defects (kinks) scales as $\kappa_1 = \sum_{k>0} \langle \hat{\gamma}_k^\dagger(\tau_Q) \hat{\gamma}_k(\tau_Q) \rangle \sim \tau_Q^{-1/2}$, in agreement with the KZ mechanism for $z = \nu = 1$ [6–8, 36]. More generally, the associated number operator for defect pairs can be expressed in momentum space as $\hat{N} = \sum_{k>0} \gamma_k^\dagger(\epsilon_f) \gamma_k(\epsilon_f)$ for a given final quench depth, measured from the critical point, $\epsilon_f = g_f - g_c$. The average number of defect pairs is $\kappa_1 = \langle \hat{N} \rangle$. At fast quenches across g_c , this average scales linearly with the quench depth, $\kappa_1 \sim \epsilon_f$, in agreement with the universal fast-quench scaling for $d = \nu = 1$ [20].

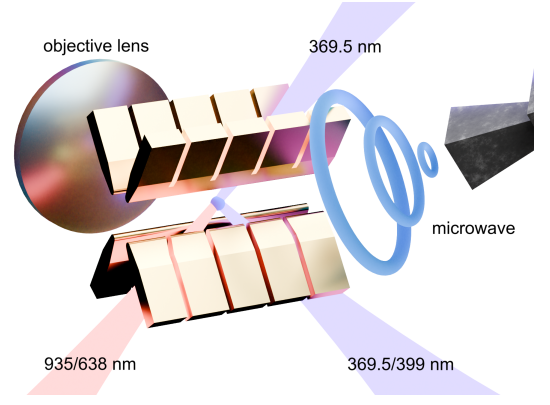


FIG. 1. Scheme of the experimental setup for controlling a single $^{171}\text{Yb}^+$ ion qubit. The ion is trapped at the center of a six-needle Paul trap (center), with surrounding control fields applied via laser beams and microwaves. Qubit initialization, manipulation, and readout are achieved using lasers at 369.5 nm, 399 nm, 638 nm, and 935 nm, focused by a high-NA (numerical aperture) objective lens (left). Microwave control is applied via near-resonant radiation around 12.442 GHz (right), with ring-shaped antenna structures indicating the drive field. The labeled laser wavelengths correspond to Doppler cooling, repumping, as well as state preparation and readout transitions.

A characterization of nonequilibrium dynamics beyond KZ is provided by the full counting statistics of defects [12–14, 18, 37–43]. The probability of observing an eigenvalue n of \hat{N} , $P(n) = \langle \delta(\hat{N} - n) \rangle$, can be characterized by cumulants, defined via the formal expansion $\log \langle e^{i\theta \hat{N}} \rangle = \sum_{q=1}^{\infty} \kappa_q (i\theta)^q / q!$. The distribution of the number of defect pairs $P(n)$ on which we focus is simply related to the distribution of the total number of defects [13], further characterized in [44]. Cumulants are functions of p_k and provided that $\sum_k p_k \gg \sum_k p_k^2$, they are proportional to the average, $\kappa_q \propto \kappa_1$. For quenches from the paramagnetic phase to the ferromagnetic phase, all κ_q share the KZ scaling, that is, $\kappa_q \propto \tau_Q^{-1/2}$ [38].

Measurement of defect statistics using real spins in quantum computers is practically infeasible due to the complexity of the spin-operator representation for any $g_f \neq 0$. In contrast, trapped-ion simulators [9, 12] provide a natural platform for directly accessing the exact defect number, enabling the first experimental investigation of fast-quench defect statistics. We explore quantum quenches of varying depth that begin near criticality and characterize the associated full counting statistics of defects. To this end, each independent TLS is modeled by an ion trap qubit implemented with a $^{171}\text{Yb}^+$ ion confined in a Paul trap consisting of six needles placed on two perpendicular planes, as shown in Fig. 1. The hyperfine clock transition in the ground state $S_{1/2}$ manifold is chosen to realize the qubit, with energy levels denoted by $|0\rangle = |F=0, m_F=0\rangle$ and $|1\rangle \equiv |F=1, m_F=0\rangle$.

Universal defect scaling. In the experimental realiza-

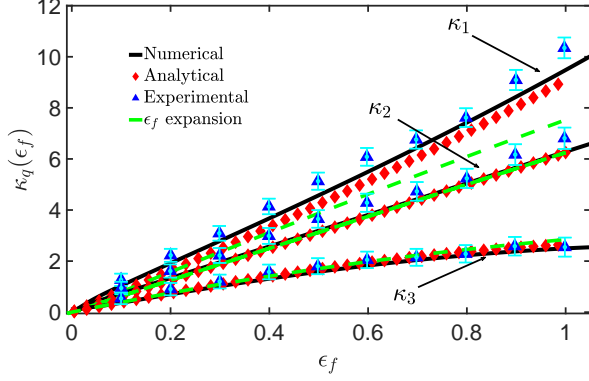


FIG. 2. First three defect pair cumulants as a function of the quench depth measured from the $\epsilon_f = 0$ to $\epsilon_f = 1$ approached from near the critical point $g_i = -1.01$. Experimentally, we use the average of the data in the fast quench region to fit the results of the numerical simulations. Numerical findings (black dots) perfectly match the analytical approximations (red circles and green dashed line) and are also in agreement with the experimental results (blue triangles) for the variance and the third cumulant. The average is only recovered in the close neighborhood of the critical point.

tion of the fast-quench dynamics, the initial transverse field is set close to the critical point, $g_i = -1.01$, choosing $\tau_Q = 0.07$ to ensure that the time evolution lies deep within the fast-quench regime. The quench depth is varied in the range $g_f \in [-1, 0]$ for a system size $N = 100$. We parameterize the final quench depth by the distance from the critical point $\epsilon_f = g_f + 1$, with $\epsilon_f \in [0, 1]$. As shown in Fig. 2, the average and variance of $P(n)$ obtained experimentally are proportional to each other and grow linearly with high precision. In contrast, the third cumulant exhibits a slower increase, consistent with stretched power-law behavior.

Next, we carry out an exact calculation of the first three cumulants of $P(n)$ for an initial coupling $g_i = -1$, and also shed light on their analytical properties by expansion in terms of the final quench depth g_f up to the second order. The fast quench limit admits a precise analytical understanding via the overlap between the initial ground state $|\text{GS}_k(g_i = -1)\rangle$ and the final excited state $|\text{ES}_k(g_f)\rangle$ in a given k -th momentum mode, $p_k = |\langle \text{GS}_k(g_i) | \text{ES}_k(g_f) \rangle|^2$. First, the low-order ϵ_f expansion of the average is tested. Although it precisely matches the numerical results in the neighborhood of the critical point, slight deviations arise from it. In contrast, the second cumulant is exactly linear in ϵ_f for arbitrary quench depths,

$$\kappa_1 \approx \frac{L}{4\pi} \left[\epsilon_f + \frac{\pi-4}{8} \epsilon_f^2 - \frac{3\pi-10}{24} \epsilon_f^3 - \frac{15\pi-48}{128} \epsilon_f^4 \right] + O(\epsilon_f^5), \quad (2)$$

$$\kappa_2 = \frac{L}{16} \epsilon_f. \quad (3)$$

The comparison of the exact analytical, numerical, and experimental results is shown in Fig. 2. Although the variance perfectly follows the linear slope, the average shows small deviations away from the critical point. To illustrate the validity regime for the fast-quench scaling of the experimental results, the numerical cumulants were obtained for the same number of modes $N = 100$ and initial transverse field $g_i = -1.01$, using a shorter quench time $\tau_Q = 0.01$, allowing a direct comparison with the exact sudden limit with $\tau_Q = 0$. We further show how a second-order expansion $g_f = 0$ with $g_i = -1.01$ provides slightly better results for the average over a broader range in [44].

Similarly to the average, the third cumulant admits a rather involved closed expression, as shown in [44]. Yet, at variance with the average, the second-order term in its ϵ_f expansion is no longer negligible. This leads to a noticeable suppression in the skewness correction,

$$\kappa_3 = \frac{L}{32\pi} \left[\epsilon_f - \frac{\pi-2}{128} \epsilon_f^2 - \frac{3\pi-10}{192} \epsilon_f^3 \right] + O(\epsilon_f^4) \quad (4)$$

where the coefficient of the quadratic term exceeds that of the linear one. This behavior, along with the agreement between the analytical, numerical, and experimental results, is also illustrated in Fig. 2. For better distinguishability, the plot shows the cumulants of the number of pairs of defects. Additional details of the exact second-order expansion of the excitation probabilities at $g_i = -1.01$ and the corresponding cumulants as a function of g_f around $g_f = 0$ are shown in [44].

As a significant consequence, the defect pair number distribution remains consistently sub-Poissonian [24, 42, 43], both in terms of variance and skewness, $\kappa_2/\kappa_1 < 1$ and $\kappa_3/\kappa_1 < 1$. In contrast to conventional critical dynamics [12–14, 38], the cumulants of the defect number become super-Poissonian, $2\kappa_2 > \kappa_1$, $4\kappa_3 > \kappa_1$, as detailed in [44]. We validate the analytical approximations by analyzing the statistics of defect pairs. In the thermodynamic limit, the transition probabilities p_k become continuous functions of k , leading to a limiting distribution that is Gaussian. This distribution is fully characterized by the first two cumulants, κ_1 and κ_2 , while the third cumulant, κ_3 , quantifies the rate at which skewness corrections vanish. As a result, the limiting distributions exhibit behavior analogous to the KZ scaling regime with a paramagnetic initial state: both the peak position and the width scale proportionally. As shown in Fig. 3, the histograms of $P(n)$ experimentally obtained closely follow Gaussian distributions, with the average and variance determined from the experimental data.

Slow-driving universality. The trapped-ion simulator also enables experimental access to the scaling of the first three cumulants in the slow-driving limit, $\tau_Q \gtrsim 1$. These quantum simulations correspond to the same initial transverse field near the critical point ($g_i = -1.01$), while keeping the final quench depth fixed, $g_f = 0$, and

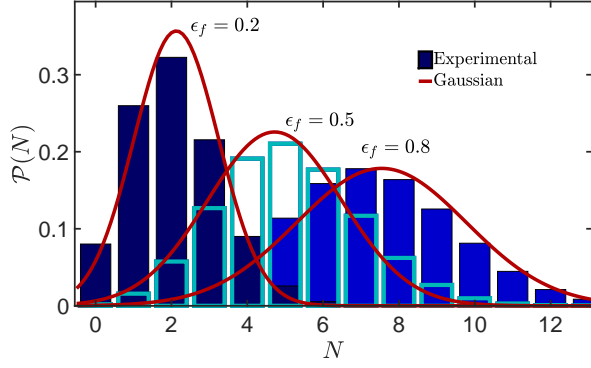


FIG. 3. Histograms of the defect pair number in sudden quenches stopping at different depths ϵ_f . With the initial value of the experimental results, $g_i = -1.01$, precise matching is displayed with the Gaussian limiting distribution.

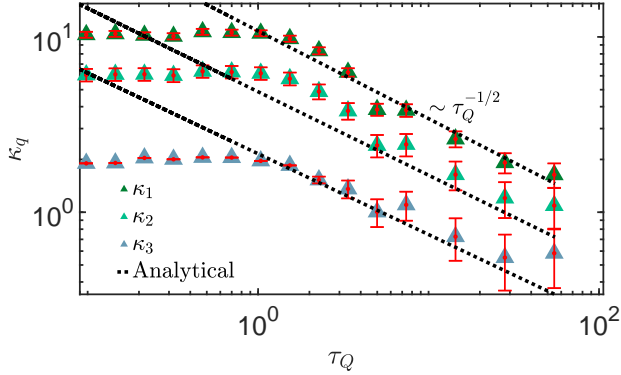


FIG. 4. Kibble-Zurek power-law scaling for the first three defect pair cumulants and their breakdown at fast quenches, validated by the analytical approximations. Up to small deviations, precise matching is displayed for the overall power-law behavior ($N = 100$ and $g_i = -1.01$ for both the experimental and numerical results).

varying τ_Q from the onset of the fast-quench limit to near-adiabatic dynamics. As shown in Fig. 4, the cumulants exhibit a characteristic crossover from a fast-quench plateau to a power-law decay, $\sim \tau_Q^{-1/2}$, in agreement with KZ scaling behavior for larger initial g_i .

To complement these experimental results, we analyze the dynamics using approximate analytical and numerical approaches. Although the exact time-evolved wavefunction for each mode can be expressed in terms of parabolic cylinder functions [24], determining their correct combination and accessing their limiting forms in the slow-driving regime remains analytically intractable. However, since the time-dependent Schrödinger equation in the leading order depends on the combination of $k^2\tau_Q$, the transition probabilities are expected to inherit this scaling behavior. This is further refined through minimal numerical input, which reveals a characteristic exponential suppression, $p_k \approx e^{-\pi k \sqrt{3\tau_Q/2}}$. The numerical

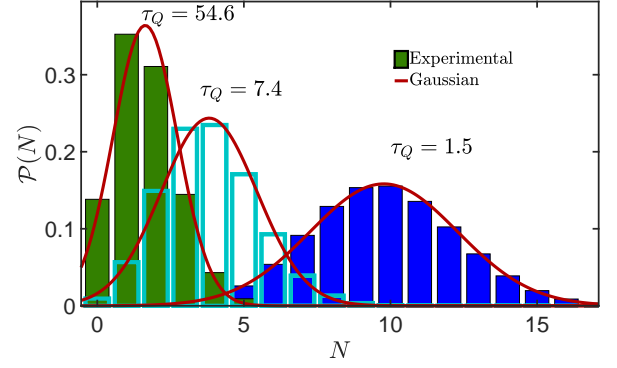


FIG. 5. Defect pair number statistics for slow driving. For smaller driving times, slight deviations are observed, while good matching is found inside the power-law scaling regime with the limiting Gaussian distribution. ($\tau_Q = 1.5, 7.4, 54.6$, $N = 100$ and $g_i = -1.01$).

validation of this ansatz is presented in Appendix .

As in the KZ scaling scenario with a large initial g_i , the dominant contribution arises from the low-momentum sector, which directly leads to the same scaling $\tau_Q^{-1/2}$ for all cumulants, albeit with different coefficients. In sharp contrast to the general sub-Poissonian behavior for large initial g_i , both in the KZ scaling regime and for fast quenches with varying g_f , the cumulant ratios increase. In particular, within the exponential approximation, one finds the approximate cumulant scaling $\kappa_1 \approx L(6\pi^4\tau_Q)^{-1/2}$, $\kappa_2 \approx L(6\pi^4\tau_Q)^{-1/2}/2$, $\kappa_3 \approx L(6\pi^4\tau_Q)^{-1/2}/3$ implying that both the variance and the skewness of the defect pair number remain sub-Poissonian, $\kappa_2 < \kappa_1$, $\kappa_3 < \kappa_1$. These analytical approximations, up to a small constant prefactor, closely match the experimental data, as illustrated in Fig. 4. Remarkably, the defect number cumulants display super-Poissonian behavior in the slow driving regime as well, as detailed in [44]. In particular, beyond the leading-order exponential approximations, small deviations break this equivalence, leading to an overall super-Poissonian character for the variance, $\kappa_1 < 2\kappa_2$, while the inequality $4\kappa_3 > \kappa_1$ is readily captured by the exponential approximation. These subtle corrections are most clearly revealed in the cumulant ratios, as detailed in [44].

Finally, the theoretical predictions and experimental results for the defect statistics are presented in Fig. 5. Within the power-law scaling regime, we observe excellent agreement between numerical simulations and analytical predictions. At shorter driving times, around $\tau_Q \sim \mathcal{O}(1)$, a fast-quench plateau emerges, leading to minor deviations; however, the general Gaussian character of the distribution remains intact.

Conclusions. We have reported the experimental verification of universal defect statistics in fast quantum quenches from a critical point, using a trapped-ion quan-

tum simulator. Beyond the experimental observations, our study provides new theoretical insights into the dynamics of quantum phase transitions. Remarkably, Gaussian defect statistics and the linear scaling of the first two cumulants with quench depth remain robust even when the quench is initiated from the critical point, with the third cumulant exhibiting a slower growth due to quadratic suppression. In the slow-driving regime, universal signatures beyond KZ scaling persist, despite the quenches starting near criticality. These findings deepen our understanding of nonequilibrium quantum critical dynamics and establish quench-depth scaling as a stringent benchmark for quantum simulators and quantum computing platforms.

Acknowledgements. This project was supported by the Luxembourg National Research Fund (FNR Grant Nos. 17132054 and 17132060), the National Key Research and Development Program of China (Grant No. 2024YFA1409403), the National Natural Science Foundation of China (Grant No. 11275233, No. 11734015, and No. 12204455) and the Innovation Program for Quantum Science and Technology (Grant No. 2021ZD0301604 and No. 2021ZD0301200).

* andras.grabarits@uni.lu

† jmcui@ustc.edu.cn

‡ zenghuabi@hainanu.edu.cn

§ hyf@ustc.edu.cn

¶ cffi@ustc.edu.cn

** adolfo.delcampo@uni.lu

†† wcx1221@mail.ustc.edu.cn

- [1] S. Sachdev, *Quantum Phase Transitions*, 2nd ed. (Cambridge University Press, 2011).
- [2] T. W. B. Kibble, Topology of cosmic domains and strings, *Journal of Physics A: Mathematical and General* **9**, 1387 (1976).
- [3] W. H. Zurek, Cosmological experiments in superfluid helium?, *Nature* **317**, 505 (1985).
- [4] W. Zurek, Cosmological experiments in condensed matter systems, *Physics Reports* **276**, 177 (1996).
- [5] A. del Campo and W. H. Zurek, Universality of phase transition dynamics: Topological defects from symmetry breaking, *International Journal of Modern Physics A* **29**, 1430018 (2014).
- [6] B. Damski, The simplest quantum model supporting the kibble-zurek mechanism of topological defect production: Landau-zener transitions from a new perspective, *Phys. Rev. Lett.* **95**, 035701 (2005).
- [7] J. Dziarmaga, Dynamics of a quantum phase transition: Exact solution of the quantum ising model, *Phys. Rev. Lett.* **95**, 245701 (2005).
- [8] W. H. Zurek, U. Dorner, and P. Zoller, Dynamics of a quantum phase transition, *Phys. Rev. Lett.* **95**, 105701 (2005).
- [9] J.-M. Cui, Y.-F. Huang, Z. Wang, D.-Y. Cao, J. Wang, W.-M. Lv, L. Luo, A. del Campo, Y.-J. Han, C.-F. Li, and G.-C. Guo, Experimental trapped-ion quantum simulation of the kibble-zurek dynamics in momentum space, *Scientific Reports* **6**, 33381 (2016).
- [10] B. Gardas, J. Dziarmaga, W. H. Zurek, and M. Zwolak, Defects in quantum computers, *Scientific Reports* **8**, 4539 (2018).
- [11] P. Weinberg, M. Tylutki, J. M. Rönkkö, J. Westerholm, J. A. Åström, P. Manninen, P. Törmä, and A. W. Sandvik, Scaling and diabatic effects in quantum annealing with a d-wave device, *Phys. Rev. Lett.* **124**, 090502 (2020).
- [12] J.-M. Cui, F. J. Gómez-Ruiz, Y.-F. Huang, C.-F. Li, G.-C. Guo, and A. del Campo, Experimentally testing quantum critical dynamics beyond the kibble-zurek mechanism, *Communications Physics* **3**, 44 (2020).
- [13] Y. Bando, Y. Susa, H. Oshiyama, N. Shibata, M. Ohzeki, F. J. Gómez-Ruiz, D. A. Lidar, S. Suzuki, A. del Campo, and H. Nishimori, Probing the universality of topological defect formation in a quantum annealer: Kibble-zurek mechanism and beyond, *Phys. Rev. Research* **2**, 033369 (2020).
- [14] A. D. King, S. Suzuki, J. Raymond, A. Zucca, T. Lanting, F. Altomare, A. J. Berkley, S. Ejtemaee, E. Hoskinson, S. Huang, E. Ladizinsky, A. J. R. MacDonald, G. Marsden, T. Oh, G. Poulin-Lamarre, M. Reis, C. Rich, Y. Sato, J. D. Whittaker, J. Yao, R. Harris, D. A. Lidar, H. Nishimori, and M. H. Amin, Coherent quantum annealing in a programmable 2,000 qubit ising chain, *Nature Physics* **18**, 1324 (2022).
- [15] B.-W. Li, Y.-K. Wu, Q.-X. Mei, R. Yao, W.-Q. Lian, M.-L. Cai, Y. Wang, B.-X. Qi, L. Yao, L. He, Z.-C. Zhou, and L.-M. Duan, Probing critical behavior of long-range transverse-field ising model through quantum kibble-zurek mechanism, *PRX Quantum* **4**, 010302 (2023).
- [16] A. Ali, H. Xu, W. Bernoudy, A. Nocera, A. D. King, and A. Banerjee, Quantum quench dynamics of geometrically frustrated ising models, *Nature Communications* **15**, 10756 (2024).
- [17] A. Miessen, D. J. Egger, I. Tavernelli, and G. Mazzola, Benchmarking digital quantum simulations above hundreds of qubits using quantum critical dynamics, *PRX Quantum* **5**, 040320 (2024).
- [18] A. D. King, A. Nocera, M. M. Rams, J. Dziarmaga, R. Wiersema, W. Bernoudy, J. Raymond, N. Kaushal, N. Heinsdorf, R. Harris, K. Boothby, F. Altomare, M. Asad, A. J. Berkley, M. Boschnak, K. Chern, H. Christiani, S. Cibere, J. Connor, M. H. Dehn, R. Deshpande, S. Ejtemaee, P. Farre, K. Hamer, E. Hoskinson, S. Huang, M. W. Johnson, S. Kortas, E. Ladizinsky, T. Lanting, T. Lai, R. Li, A. J. R. MacDonald, G. Marsden, C. C. McGeoch, R. Molavi, T. Oh, R. Neufeld, M. Norouzpour, J. Pasvolsky, P. Poitras, G. Poulin-Lamarre, T. Prescott, M. Reis, C. Rich, M. Samani, B. Sheldan, A. Smirnov, E. Sterpka, B. T. Clavera, N. Tsai, M. Volkmann, A. M. Whitar, J. D. Whittaker, W. Wilkinson, J. Yao, T. J. Yi, A. W. Sandvik, G. Alvarez, R. G. Melko, J. Carrasquilla, M. Franz, and M. H. Amin, Beyond-classical computation in quantum simulation, *Science* **388**, 199 (2025).
- [19] T. Zhang, H. Wang, W. Zhang, Y. Wang, A. Du, Z. Li, Y. Wu, C. Li, J. Hu, H. Zhai, and W. Chen, *Observation of near-critical kibble-zurek scaling in rydberg atom arrays* (2025), [arXiv:2505.07930 \[cond-mat.quant-gas\]](https://arxiv.org/abs/2505.07930).
- [20] H.-B. Zeng, C.-Y. Xia, and A. del Campo, Universal breakdown of kibble-zurek scaling in fast quenches across

- a phase transition, *Phys. Rev. Lett.* **130**, 060402 (2023).
- [21] C.-Y. Xia, H.-B. Zeng, C.-M. Chen, and A. del Campo, Structural phase transition and its critical dynamics from holography, *Phys. Rev. D* **108**, 026017 (2023).
- [22] H.-C. Kou and P. Li, Varying quench dynamics in the transverse ising chain: The kibble-zurek, saturated, and presaturated regimes, *Phys. Rev. B* **108**, 214307 (2023).
- [23] C.-Y. Xia, H.-B. Zeng, A. Grabarits, and A. del Campo, Kibble-zurek mechanism and beyond: Lessons from a holographic superfluid disk (2024), [arXiv:2406.09433 \[cond-mat.stat-mech\]](#).
- [24] A. Grabarits, F. Balducci, and A. del Campo, Driving a quantum phase transition at an arbitrary rate: Exact solution of the transverse-field ising model, *Phys. Rev. A* **111**, 042207 (2025).
- [25] S. Ejtemaee and P. C. Haljan, Spontaneous nucleation and dynamics of kink defects in zigzag arrays of trapped ions, *Phys. Rev. A* **87**, 051401 (2013).
- [26] S. Ulm, J. Roßnagel, G. Jacob, C. Degünther, S. T. Dawkins, U. G. Poschinger, R. Nigmatullin, A. Retzker, M. B. Plenio, F. Schmidt-Kaler, and K. Singer, Observation of the Kibble-Zurek scaling law for defect formation in ion crystals, *Nat. Comm.* **4**, 2290 (2013).
- [27] K. Pyka, J. Keller, H. L. Partner, R. Nigmatullin, T. Burgermeister, D. M. Meier, K. Kuhlmann, A. Retzker, M. B. Plenio, W. H. Zurek, A. del Campo, and T. E. Mehlstäubler, Topological defect formation and spontaneous symmetry breaking in ion Coulomb crystals, *Nat. Comm.* **4**, 2291 (2013).
- [28] X. Rao, Y. Liu, M. Li, T. Liu, H. Zeng, and L. Luo, Verified universal breakdown of kibble-zurek scaling in fast quenches (2025), [arXiv:2506.06841 \[quant-ph\]](#).
- [29] B. Ko, J. W. Park, and Y. Shin, Kibble-zurek universality in a strongly interacting fermi superfluid, *Nature Physics* **15**, 1227 (2019).
- [30] S. Donadello, S. Serafini, T. Bienaimé, F. Dalfovo, G. Lamporesi, and G. Ferrari, Creation and counting of defects in a temperature-quenched bose-einstein condensate, *Phys. Rev. A* **94**, 023628 (2016).
- [31] J. Goo, Y. Lim, and Y. Shin, Defect saturation in a rapidly quenched bose gas, *Phys. Rev. Lett.* **127**, 115701 (2021).
- [32] J. Goo, Y. Lee, Y. Lim, D. Bae, T. Rabga, and Y. Shin, Universal early coarsening of quenched bose gases, *Phys. Rev. Lett.* **128**, 135701 (2022).
- [33] A. del Campo, G. De Chiara, G. Morigi, M. B. Plenio, and A. Retzker, Structural defects in ion chains by quenching the external potential: The inhomogeneous kibble-zurek mechanism, *Phys. Rev. Lett.* **105**, 075701 (2010).
- [34] A. Chandran, A. Erez, S. S. Gubser, and S. L. Sondhi, Kibble-zurek problem: Universality and the scaling limit, *Phys. Rev. B* **86**, 064304 (2012).
- [35] S. Suzuki, J. Inoue, and B. Chakrabarti, *Quantum Ising Phases and Transitions in Transverse Ising Models*, Lecture Notes in Physics (Springer, 2012).
- [36] J. Dziarmaga, Dynamics of a quantum phase transition and relaxation to a steady state, *Advances in Physics* **59**, 1063 (2010).
- [37] L. Cincio, J. Dziarmaga, M. M. Rams, and W. H. Zurek, Entropy of entanglement and correlations induced by a quench: Dynamics of a quantum phase transition in the quantum ising model, *Phys. Rev. A* **75**, 052321 (2007).
- [38] A. del Campo, Universal statistics of topological defects formed in a quantum phase transition, *Phys. Rev. Lett.* **121**, 200601 (2018).
- [39] D. Subires, F. J. Gómez-Ruiz, A. Ruiz-García, D. Alonso, and A. del Campo, Benchmarking quantum annealing dynamics: The spin-vector langevin model, *Phys. Rev. Res.* **4**, 023104 (2022).
- [40] S. Gherardini, L. Buffoni, and N. Defenu, Universal defects statistics with strong long-range interactions, *Phys. Rev. Lett.* **133**, 113401 (2024).
- [41] O. Kiss, D. Teplitskiy, M. Grossi, and A. Mandarino, Statistics of topological defects across a phase transition in a digital superconducting quantum processor, *Quantum Science and Technology* **10**, 035037 (2025).
- [42] A.-M. Visuri, A. G. Cadavid, B. A. Bhargava, S. V. Romero, A. Grabarits, P. Chandarana, E. Solano, A. del Campo, and N. N. Hegade, Digitized counterdiabatic quantum critical dynamics (2025), [arXiv:2502.15100 \[quant-ph\]](#).
- [43] A. Grabarits and A. del Campo, Universal defect statistics in counterdiabatic quantum critical dynamics (2025), [arXiv:2503.22212 \[quant-ph\]](#).
- [44] url will be inserted by publisher, .

TFQIM diagonalization

With periodic boundary conditions, $\hat{\sigma}_1^z = \hat{\sigma}_{N+1}^z$, the TFQIM is translationally invariant and can be diagonalized using standard techniques. By performing a Jordan-Wigner transformation and a subsequent Fourier-mode decomposition, it can be written in the form $H = \sum_{k>0} H_k$ where the single-mode Hamiltonian $H_k = \hat{\varphi}_k^\dagger [(g - \cos k)\sigma^z + \sin k\sigma^x] \hat{\varphi}_k$ as defined in the main text has eigenvalues $\epsilon_k(g) = 2\sqrt{1 + g^2 - 2g \cos k}$. The ground state at an initial arbitrary g_i is given by

$$|\text{GS}_k(g_i = -1)\rangle = \frac{(g_i - \cos k - \sqrt{1 + g_i^2 - 2g_i \cos k}, \sin k)^T}{\sqrt{\sin^2 k + (g_i - \cos k - \sqrt{1 + g_i^2 - 2g_i \cos k})^2}}. \quad (5)$$

The excited state in each mode for arbitrary g_f reads

$$|\text{ES}_k(g_f)\rangle = \frac{(g_f - \cos k + \sqrt{1 + g_f^2 - 2g_f \cos k}, \sin k)^T}{\sqrt{\sin^2 k + (g_f - \cos k + \sqrt{1 + g_f^2 - 2g_f \cos k})^2}}. \quad (6)$$

From this, the general expression for the excitation probabilities is given by

$$\begin{aligned} p_k^{fi} &= |\langle \text{ES}_k(g_f) | \text{GS}_k(g_i) \rangle|^2 \\ &= \frac{1}{\sin^2 k + (g_f - \cos k + \sqrt{1 + g_f^2 - 2g_f \cos k})^2} \frac{1}{\sin^2 k + (g_i - \cos k - \sqrt{1 + g_i^2 - 2g_i \cos k})^2} \\ &\quad \times \left[\sin^4 k + 2 \sin^2 k \left(g_i - \cos k - \sqrt{1 + g_i^2 - 2g_i \cos k} \right) \left(g_f - \cos k + \sqrt{1 + g_f^2 - 2g_f \cos k} \right) \right. \\ &\quad \left. + \left(g_i - \cos k - \sqrt{1 + g_i^2 - 2g_i \cos k} \right)^2 \left(g_f - \cos k + \sqrt{1 + g_f^2 - 2g_f \cos k} \right)^2 \right]. \end{aligned} \quad (7)$$

Derivation of the fast quench cumulants

In this section, we derive the formulas for the exact fast-quench cumulants and their expansion around both $g_f = 0$ and $\epsilon_f = 0$. Starting from the critical point, $g_i = -1$, it can be shown that the ground state can be expressed as

$$|\text{GS}_k(g_i = -1)\rangle = \begin{pmatrix} -\cos(k/4) \\ \sin(k/4) \end{pmatrix}, \quad (8)$$

with eigenvalue of $-2\cos(k/2)$. and the exact excitation probabilities read

$$\begin{aligned} p_k &= |\langle \text{ES}_k(g_f) | \text{GS}_k(g_i = -1) \rangle|^2 \\ &= \frac{\sin^2 k \sin^2 \frac{k}{4} + \cos^2 \frac{k}{4} \left(g_f - \cos k + \sqrt{1 + g_f^2 - 2g_f \cos k} \right)^2 - \sin k \sin \frac{k}{2} \left(g_f - \cos k + \sqrt{1 + g_f^2 - 2g_f \cos k} \right)}{\sin^2 k + \left(g_f - \cos k + \sqrt{1 + g_f^2 - 2g_f \cos k} \right)^2}. \end{aligned} \quad (9)$$

We start with the average within the integral approximation $\kappa_1 = 2 \sum_{k>0} p_k \approx (L/\pi) \int_0^\pi dk p_k$. By straightforward computation, it can be seen that the excitation probabilities in Eq. (9) with $g_i = -1$ can be expressed in a convenient form as

$$p_k = \frac{\sin^2 \frac{k}{4}}{2} \left(1 - \frac{g_f - \cos k}{\sqrt{1 + g_f^2 - 2g_f \cos k}} \right) + \frac{\cos^2 \frac{k}{4}}{2} \left(1 + \frac{g_f - \cos k}{\sqrt{1 + g_f^2 - 2g_f \cos k}} \right) - \frac{1}{2} \frac{\sin k \sin \frac{k}{2}}{\sqrt{1 + g_f^2 - 2g_f \cos k}} \quad (10)$$

As a result, the average can be expressed as

$$\begin{aligned}
\kappa_1 &\approx \frac{L}{2\pi} \int_0^\pi dk \frac{\sin^2 \frac{k}{4}}{2} \left(1 - \frac{g_f - \cos k}{\sqrt{1 + g_f^2 - 2g_f \cos k}} \right) + \frac{\cos^2 \frac{k}{4}}{2} \left(1 + \frac{g_f - \cos k}{\sqrt{1 + g_f^2 - 2g_f \cos k}} \right) - \frac{1}{2} \frac{\sin k \sin \frac{k}{2}}{\sqrt{1 + g_f^2 - 2g_f \cos k}} \\
&= \frac{L}{4\pi} \int_0^\pi dk \left[1 + \frac{\cos \frac{k}{2} (g_f - \cos k) - \sin k \sin \frac{k}{2}}{\sqrt{1 + g_f^2 - 2g_f \cos k}} \right] = \frac{L}{2} + \frac{L}{\sqrt{8\pi^2}} \int_{-1}^1 dt \frac{\sqrt{1+t}(g_f - t) - \sqrt{1-t}\sqrt{1-t^2}}{\sqrt{1-t^2}\sqrt{1+g_f^2 - 2g_f t}} \\
&= \frac{L}{4} - \frac{L}{4\pi} (1 - g_f) \frac{\arcsin \left(\frac{2\sqrt{-g_f}}{1-g_f} \right)}{\sqrt{-g_f}},
\end{aligned}$$

valid for $g_f < 0$. Expanding up to the fifth order, it becomes apparent that for $g_f \in [-1, 0]$ the average is dominated by the linear order

$$\kappa_1 = \frac{L}{2\pi} \left(\frac{\pi - 2}{2} + \frac{2}{3}g_f + \frac{2}{15}g_f^2 + \frac{2}{35}g_f^3 + \frac{2}{64}g_f^4 + \frac{2}{99}g_f^5 + \dots \right). \quad (11)$$

This expression is further expressed in terms of the distance from the critical point, $g_c = -1$, $\epsilon_f = 1 + g_f$, leading to

$$\kappa_1 \approx \frac{L}{4} - \frac{L}{4\pi} (2 - \epsilon_f) \frac{\arcsin \left(\frac{2\sqrt{1-\epsilon_f}}{2-\epsilon_f} \right)}{\sqrt{1-\epsilon_f}}. \quad (12)$$

A more compact expansion scheme follows with ϵ_f , yielding

$$\kappa_1 \approx \frac{L}{4\pi} \left[\epsilon_f + \frac{\pi - 4}{8} \epsilon_f^2 - \frac{3\pi - 10}{24} \epsilon_f^3 - \frac{3(5\pi - 16)}{128} \epsilon_f^4 - \frac{105\pi - 332}{960} \epsilon_f^5 + \dots \right]. \quad (13)$$

For the variance, the individual Bernoulli variances can be written as

$$p_k(1 - p_k) = \frac{1}{4} \left[1 - \frac{(\cos \frac{k}{2} (g_f - \cos k) - \sin k \sin \frac{k}{2})^2}{1 + g_f^2 - 2g_f \cos k} \right]. \quad (14)$$

Thus, summing up the individual variances results in

$$\begin{aligned}
\kappa_2 &\approx \frac{L}{2\pi} \int_0^\pi dk \frac{1}{4} \left[1 - \frac{(\cos \frac{k}{2} (g_f - \cos k) - \sin k \sin \frac{k}{2})^2}{1 + g_f^2 - 2g_f \cos k} \right] = \frac{L}{2} - \frac{L}{4\pi} \int_{-1}^1 dt \frac{[\sqrt{1+t}(g_f - t) - \sqrt{1-t}\sqrt{1-t^2}]^2}{\sqrt{1-t^2}(1+t^2-2g_f t)} \quad (15) \\
&= \frac{L}{8} - \frac{L}{16\pi} (g_f - 1)^2 \int_{-1}^1 dt \frac{\sqrt{1+t}}{\sqrt{1-t}(1+g_f^2-2g_f t)} = \frac{L}{8} - \frac{L}{16} (g_f - 1)^2 \frac{1}{(1-g_f)} = \frac{L}{8} - \frac{L}{16} (1 - g_f) = \frac{L}{16} + \frac{L}{16} g_f,
\end{aligned}$$

which, in terms of the distance from the critical point, becomes

$$\kappa_2 \approx \frac{L}{16} \epsilon_f. \quad (16)$$

Finally, the third cumulant can also be obtained exactly, but in a rather involved form, similar to the average,

$$p_k(1 - p_k)(1 - 2p_k) = \frac{1}{4} \left[1 - \frac{(\cos \frac{k}{2} (g_f - \cos k) - \sin k \sin \frac{k}{2})^2}{1 + g_f^2 - 2g_f \cos k} \right] \frac{\sin k \sin \frac{k}{2} - \cos \frac{k}{2} (g_f - \cos k)}{\sqrt{1 + g_f^2 - 2g_f \cos k}}, \quad (17)$$

which leads to the integral of

$$\kappa_3 \approx \frac{L}{2\pi} \int_0^\pi dk \frac{1}{4} \left[\frac{\sin k \sin \frac{k}{2} - \cos \frac{k}{2} (g_f - \cos k)}{\sqrt{1 + g_f^2 - 2g_f \cos k}} + \frac{(\cos \frac{k}{2} (g_f - \cos k) - \sin k \sin \frac{k}{2})^3}{(1 + g_f^2 - 2g_f \cos k)^{3/2}} \right] \quad (18)$$

$$\begin{aligned} &= \frac{L}{8\pi} \int_{-1}^1 dt \frac{g_f - 1}{\sqrt{2}\sqrt{1-t}\sqrt{1+g_f^2-2g_ft}} + \frac{(\sqrt{1+t}(g_f-t) - \sqrt{1-t}\sqrt{1-t^2})^3}{\sqrt{8}\sqrt{1-t^2}(1+g_f^2-2g_ft)^{3/2}} \\ &= \frac{L}{8\pi} (1-g_f) \frac{\arcsin\left(\frac{2\sqrt{-g_f}}{1-g_f}\right)}{\sqrt{-g_f}} + \frac{L}{\sqrt{256}\pi^2} (g_f-1)^3 \int_{-1}^1 dt \frac{1+t}{\sqrt{1-t}(1+g_f^2-2g_ft)^{3/2}} \\ &= \frac{L}{8\pi} (1-g_f) \frac{\arcsin\left(\frac{2\sqrt{-g_f}}{1-g_f}\right)}{\sqrt{-g_f}} + \frac{L}{64\pi} \left[\frac{\arccos\left(\frac{g_f^2+6g_f+1}{(1-g_f)^2}\right)}{\sqrt{-g_f^3}} (g_f-1)^3 + 4 \frac{1-g_f^2}{g_f} \right]. \end{aligned} \quad (19)$$

$$(20)$$

The leading order expansion in terms of g_f reads

$$\kappa_3 \approx \frac{L}{8\pi} \left(\frac{2}{3} - \frac{4}{15} g_f - \frac{4}{21} g_f^2 - \frac{4}{63} g_f^3 - \frac{116}{3465} g_f^4 - \frac{188}{9009} g_f^5 + \dots \right), \quad (21)$$

In terms of the distance for the critical point, the leading-order behavior takes the form of

$$\kappa_3 = \frac{L}{32\pi} \left[\epsilon_f - \frac{\pi-2}{128} \epsilon_f^2 - \frac{3\pi-10}{192} \epsilon_f^3 + \frac{48-15\pi}{1024\pi} \epsilon_f^4 + \frac{332-105\pi}{7720} \epsilon_f^5 + \dots \right]. \quad (22)$$

Expansion at small initial transverse fields

In this appendix, we provide a second-order expansion of the excitation probabilities in Eq. (7):

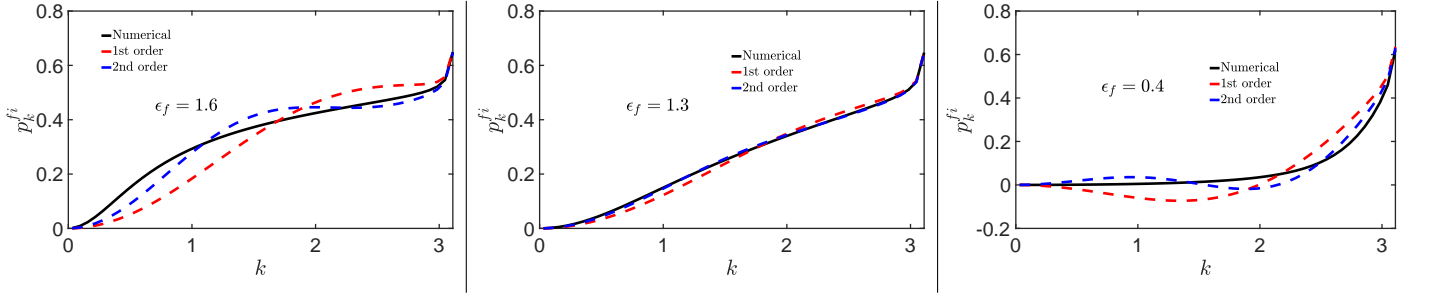


FIG. 6. Excitation probabilities up to second order in g_f for the experimental value of the initial value of $g_i = -1.01$ as a function of k for $\epsilon_f = 1.6, 1.3, 0.4$. Approaching the critical points, the precision and accuracy deteriorate gradually.

$$\begin{aligned}
p_k^{f_i} = & \frac{4 \sin^4 \frac{k}{2} \left(-g_i + \cos k + \sqrt{1 + g_i^2 - 2g_i \cos k} \right)^2 + 4 \left(-g_i + \cos k + \sqrt{1 + g_i^2 - 2g_i \cos k} \right) \sin^2 \frac{k}{2} \sin^2 k + \sin^4 k}{((1 - \cos k)^2 + \sin^2 k) \left(\left(g_i - \cos k - \sqrt{1 + g_i^2 - 2g_i \cos k} \right)^2 + \sin^2 k \right)} \\
& + g_f \left(\frac{4 \sin^4 \frac{k}{2} \left(-g_i + \cos k + \sqrt{1 + g_i^2 - 2g_i \cos k} \right)^2 + 4 \sin^2 \frac{k}{2} \left(-g_i + \cos k + \sqrt{1 + g_i^2 - 2g_i \cos k} \right) \sin^2 k}{\left(\left(g_i - \cos k - \sqrt{1 + g_i^2 - 2g_i \cos k} \right)^2 + \sin^2 k \right) ((1 - \cos k)^2 + \sin^2 k)} \right. \\
& \left. - \frac{32 \sin^6 \frac{k}{2} \left(\sin^2 \frac{k}{2} \left(-g_i + \cos k + \sqrt{1 + g_i^2 - 2g_i \cos k} \right)^2 + \left(-g_i + \cos k + \sqrt{1 + g_i^2 - 2g_i \cos k} \right) \sin k^2 + \sin^4 k \right)}{\left(\left(g_i - \cos k - \sqrt{1 + g_i^2 - 2g_i \cos k} \right)^2 + \sin^2 k \right) ((1 - \cos k)^2 + \sin^2 k)^2} \right) \\
& + g_f^2 \left(- \frac{32 \sin^6 \frac{k}{2} \left(2 \sin^2 \frac{k}{2} \left(-g_i + \cos k + \sqrt{1 + g_i^2 - 2g_i \cos k} \right)^2 + \left(-g_i + \cos k + \sqrt{1 + g_i^2 - 2g_i \cos k} \right) \sin k^2 \right)}{((1 - \cos k)^2 + \sin^2 k)^2 \left(\left(g_i - \cos k - \sqrt{1 + g_i^2 - 2g_i \cos k} \right)^2 + \sin^2 k \right)} \right. \\
& + \frac{(2 - 3 \cos k + \cos k^3) \left(-g_i + \cos k + \sqrt{1 + g_i^2 - 2g_i \cos k} \right)^2 + (-1 + \cos k^2) \left(-g_i + \cos k + \sqrt{1 + g_i^2 - 2g_i \cos k} \right) \sin k^2}{((1 - \cos k)^2 + \sin^2 k) \left(\left(g_i - \cos k - \sqrt{1 + g_i^2 - 2g_i \cos k} \right)^2 + \sin^2 k \right)} \\
& + \frac{\left(4 \sin^4 \frac{k}{2} \left(-g_i + \cos k + \sqrt{1 + g_i^2 - 2g_i \cos k} \right)^2 + 4 \sin^2 \frac{k}{2} \left(-g_i + \cos k + \sqrt{1 + g_i^2 - 2g_i \cos k} \right) \sin k^2 + \sin^4 k \right)}{\left(\left(g_i - \cos k - \sqrt{1 + g_i^2 - 2g_i \cos k} \right)^2 + \sin^2 k \right) ((1 - \cos k)^2 + \sin^2 k)} \\
& \left. \times \frac{\left(\frac{4(-1 + \cos k)^4}{((1 - \cos k)^2 + \sin^2 k)^2} - \frac{2 - 3 \cos k + \cos k^3}{(1 - \cos k)^2 + \sin^2 k} \right)}{\left(\left(g_i - \cos k - \sqrt{1 + g_i^2 - 2g_i \cos k} \right)^2 + \sin^2 k \right) ((1 - \cos k)^2 + \sin^2 k)} \right). \tag{23}
\end{aligned}$$

Despite the cumbersome expression, a precise matching is provided by the second-order expansion in terms of g_f in the interval $g_f \in [-0.6, 0.6]$, as displayed in Fig. 6. The corresponding cumulants are also precisely reproduced up to $\epsilon_f \approx 0.2$, as shown in Fig. 7 with coefficients being close to the $g_i = -1$ expansion results. The numerical integrals of the k dependent prefactors provide the prefactor for the cumulant expansions in the main text.

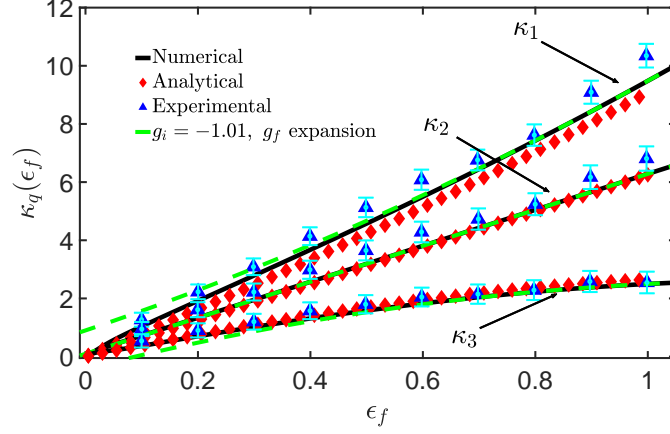


FIG. 7. First three cumulants as a function of the quench depth. A precise agreement is found for the second-order g_f expansion with the experimental, numerical, and exact analytical results for $g_i = -1$.

Demonstration of the approximate exponential excitation probabilities

In this section, we show the numerical verification of the exponential ansatz for the excitation probabilities, $p_k \sim e^{-\pi\sqrt{3\tau_Q/2}k}$. In Fig. 8 we show that this ansatz provides a precise fitting for p_k , since for different values τ_Q an accurate scaling collapse is displayed as a function of $k\sqrt{\tau_Q}$ following an exponential decay for low momenta. Within its domain of validity, this approximation contains the largest contribution to defect production, $p_k \gtrsim 5 \times 10^{-4}$.

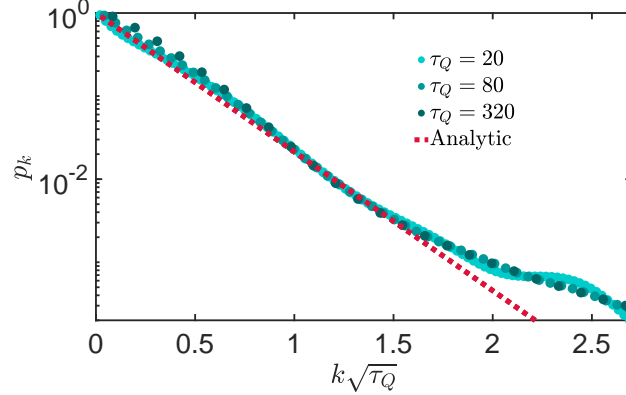


FIG. 8. Excitation probabilities in the slow driving limit for different values of τ_Q , exhibiting an approximate exponential decay, captured by the fitting in a semilog plot.

Defect number cumulant ratios

In this section, we demonstrate that the cumulants of the defect numbers become super-Poissonian both in the fast and slow driving regimes. Using the exact results and leading-order expansions in the fast quench regime, it can be shown that the variance preserves its super-Poissonian behavior as $2\kappa_1 - 4\kappa_2 \approx (1/(2\pi) - 1/4)\epsilon_f < 0 \Rightarrow 2\kappa_2/\kappa_1 > 1$, for the range of validity of the linear ϵ_f expansions. For larger values of ϵ_f , the exact solution for κ_1 reveals the same super-Poissonian behavior. The skewness ratio follows straightforwardly from the analytical approximations, following a super-Poissonian curve for the dominant range of ϵ_f . However, at the same time, it clearly converges to unity as $\epsilon_f = 1$ is reached, implying a Poissonian character. The full dependence of these cumulant ratios on ϵ_f is presented in Fig. 9.

The τ_Q dependence of the cumulant ratios is shown in Fig. 10. Although the cumulants are well-captured by KZ-like power laws, constant-factor deviations become apparent in the cumulant ratios and eventually lead to an

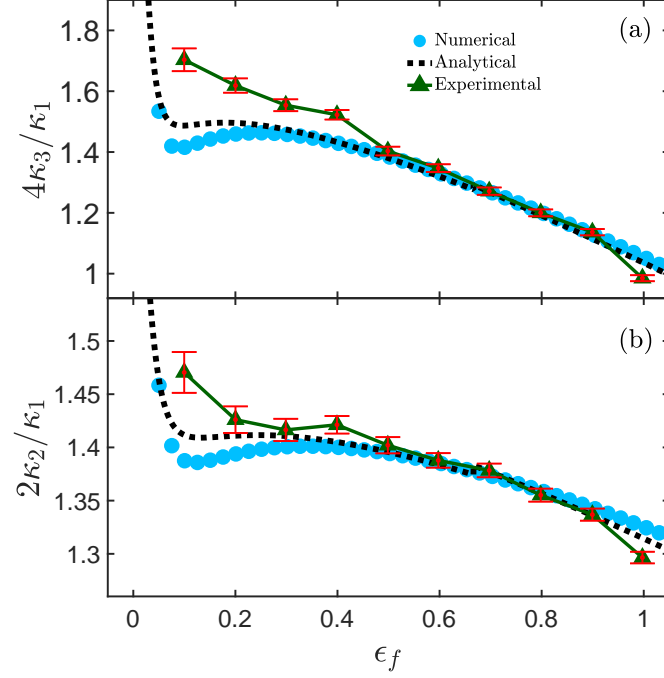


FIG. 9. Cumulant ratios of defect numbers by experimental results, numerical simulations, and analytical formulas. In all three data sets, the defect number statistics is super-Poissonian for both the variance and the skewness. (a) Skewness ratio with super-Poissonian behavior converging to the Poissonian value at $\epsilon_f = 1$. (b) Variance ratio, displaying a clear super-Poissonian behavior for the full range of ϵ_f ($\tau_Q = 0.01$ and $N = 100$).

overall super-Poissonian behavior. As shown in Fig. 10(a), the ratio of skewness exhibits well the transition to super-Poissonian, closely matching the theoretical prediction for the exponential approximation, $4\kappa_3/\kappa_1 \approx 1.5$. On the other hand, the variance ratio in panel (b) shows slight deviations from the predicted Poissonian behavior based on the exponential approximation, as upon increasing τ_Q , it shifts to a slightly larger value, $2\kappa_2/\kappa_1 \approx 1.3$, tracing out a clear super-Poissonian behavior.

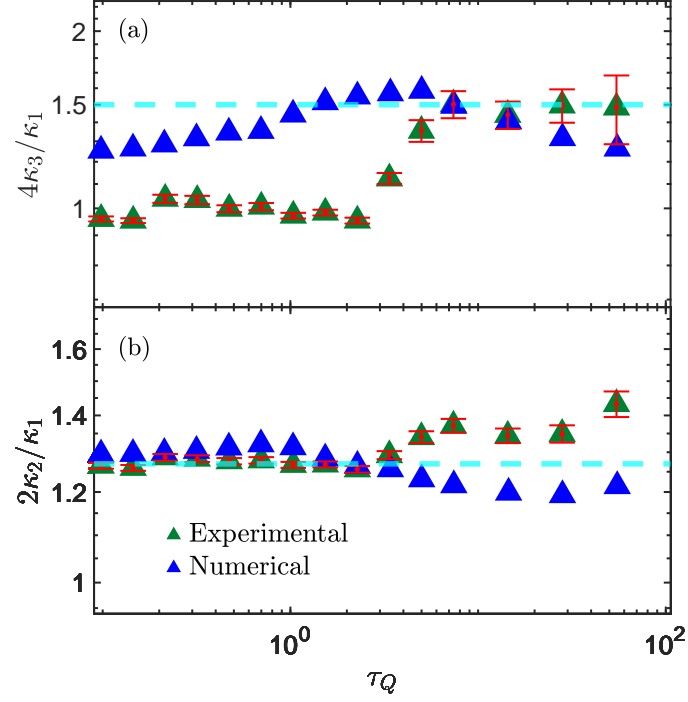


FIG. 10. Defect number cumulant ratios with varying driving time and for $\epsilon_f = 1$, exhibiting an approximately constant, super-Poissonian behavior. (a) The experimental results for the skewness ratio, besides small deviations from the numerical findings, closely match the predicted constant value, $\kappa_3/\kappa_1 \approx 1.5$ in the slow limit, while it converges to unity for fast quenches. (b) The variance ratio exhibits a slightly larger value than the one predicted by the exponential approximation, $2\kappa_2/\kappa_1 \approx 1.3$ ($\tau_Q = 0.01$ and $N = 100$).